

## Is a complete Mueller matrix necessary in biomedical imaging?

TATIANA NOVIKOVA<sup>1,2,\*</sup>  AND JESSICA C. RAMELLA-ROMAN<sup>2,3</sup>

<sup>1</sup>LPICM, CNRS, Ecole Polytechnique, IP Paris, Palaiseau, 91128, France

<sup>2</sup>Department of Biomedical Engineering, College of Engineering and Computing, Florida International University, 10555 West Flagler Street, Miami, Florida 33174, USA

<sup>3</sup>Department of Ophthalmology, Herbert Wertheim College of Medicine, Florida International University, 11200 SW 8th Street, Miami, Florida 33199, USA

\*Corresponding author: [tatiana.novikova@polytechnique.edu](mailto:tatiana.novikova@polytechnique.edu)

Received 22 July 2022; revised 17 September 2022; accepted 6 October 2022; posted 6 October 2022; published 20 October 2022

The advent of imagers with integrated linear polarization selectivity opens new opportunities for researchers interested in the polarization properties of biological tissues. In this Letter, we explore the mathematical framework necessary to obtain common parameters of interest: azimuth; retardance; and depolarization with reduced Mueller matrices that can be measured with the new instrumentation. We show that in the case of acquisition close to the tissue normal, simple algebraic analysis of the reduced form of the Mueller matrix yields results very close to those obtained with more complex decomposition algorithms applied to a complete Mueller matrix. © 2022 Optica Publishing Group

<https://doi.org/10.1364/OL.471239>

Polarization-based optical imaging techniques have found an important place in biomedical diagnosis of tissue. Mueller polarimeters implemented in reflection configuration were used for the detection of cervical pre-cancer [1], skin cancer [2], colon cancer staging [3], and risk of pre-term labor [4], to name a few.

The Mueller matrix (MM) formalism is a powerful framework for a complete description of sample's properties that alter polarization of a probing beam [5]. However, it is difficult to interpret and obtain a physical insight into all 16 coefficients of a MM. That is why the non-linear MM data compression algorithms are often used to obtain the more familiar quantities of retardance (birefringence), diattenuation (dichroism), and depolarization. Lu and Chipman [6] proved that any physically realizable MM [7] can be represented as a product of MMs of a diattenuator  $\mathbf{M}_D$ , a retarder  $\mathbf{M}_R$ , and a depolarizer  $\mathbf{M}_\Delta$  [5]:

$$\mathbf{M} = \mathbf{M}_\Delta \mathbf{M}_R \mathbf{M}_D. \quad (1)$$

The Lu–Chipman polar decomposition (LCPD) of a MM is a widely used algorithm for analyzing Mueller matrix images of biological tissues. It is common to acquire polarimetric images close to normal reflection, where  $\mathbf{M}_D$  is close to the identity matrix  $\mathbf{I}$ , as the Fresnel reflection coefficients are equal for both  $s$ - and  $p$ - components of polarized light [8]. The effect of polarizance [5] in biological tissue may become important when imaging at grazing incidence but is negligible at the normal [9]. Consequently, the MM of a depolarizer becomes

diagonal,  $\mathbf{M}_\Delta = \text{diag}(1, d_1, d_2, d_3)$ , where  $d_1, d_2$  represent linear depolarization,  $d_3$  represents a circular one. No significant optical activity (i.e., circular birefringence [5]) was observed in a majority of biological tissues [3,4,9]. Hence, Eq. (1) can be written as

$$\mathbf{M} = \begin{bmatrix} 1 & 0 & 0 & 0 \\ 0 & d_1(c^2 + s^2 \cos R) & d_1 c s(1 - \cos R) & -d_1 s \sin R \\ 0 & d_2 c s(1 - \cos R) & d_2(s^2 + c^2 \cos R) & d_2 c \sin R \\ 0 & d_3 s \sin R & -d_3 c \sin R & d_3 \cos R \end{bmatrix}, \quad (2)$$

where  $R$  is the value of scalar linear retardance,  $\theta_R$  the azimuth of the optical axis of a linear retarder,  $c = \cos(2\theta_R)$ ,  $s = \sin(2\theta_R)$ . It was demonstrated that with a commercially available polarization camera, the  $3 \times 4$  MM could be measured without rotating elements or electrically driven liquid crystals (LCs) with a compact hand-held instrument [8,10]. Qi *et al.* reported on an endoscope utilizing  $3 \times 3$  reduced MM and its decomposition [11], the reconstruction of complete MM from 12 elements was reported in Ref. [12]. These approaches reduce instrument complexity, measurement time (a weak point for the systems with rotating elements), and remove the thermal instability inherent for the LC-based polarimeters. The natural question arises: can we extract the values of scalar linear retardance, the azimuth of the optical axis, and the depolarization properties of a biological sample by measuring only part of its MM? Performing 12 measurements, we may obtain the first three rows of a MM and calculate the following quantities:

$$\theta_R = 0.5 \arctan \left( \frac{-m_{24} m_{32}}{m_{34} m_{23}} \right), \quad (3)$$

$$R = 2 \arctan \left( \frac{sm_{34} m_{23} - cm_{24} m_{32}}{2cs(m_{33} m_{23} + m_{22} m_{32})} \right), \quad (4)$$

$$d_1 = -m_{24} / (s \sin R), \quad (5)$$

$$d_2 = m_{34} / (c \sin R). \quad (6)$$

Assuming the isotropy of linear depolarization ( $d_1 = d_2 = d$ ), Eqs. (3)–(6) can be simplified as

$$\theta_R = 0.5 \arctan (-m_{24} / m_{34}) = AoP, \quad (7)$$

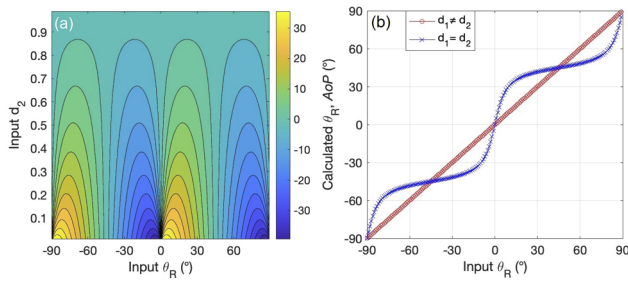


**Fig. 1.** (a) Two-dimensional (2D) map of calculated  $(\theta_R - AoP)$  values at different input values of parameters  $\theta_R$  and  $d_2$ ; (b) calculated values of  $\theta_R$  (red circles) and  $AoP$  (blue crosses) for  $d_2 = 0.5$ . Input linear retardance  $R=90^\circ$ ,  $d_1 = 0.99$ .

$$d \sin R = \sqrt{(m_{34}^2 + m_{24}^2)}. \quad (8)$$

In such a case, using a right and left circularly polarized light source and a polarized camera as a detector and performing only two measurements, both quantities calculated with Eqs. (7) and (8) can be measured with a Stokes polarimeter [13]. The first parameter [Eq. (7)] is called the angle of polarization ( $AoP$ ) and the second [Eq. (8)], the degree of linear polarization.

To test the validity of Eqs. (3)–(8) first, we simulated the MMs of an optical element composed of a serial assembly of a linear retarder and diagonal depolarizer with values of the azimuth of the optical axis varying from  $-90^\circ$  to  $90^\circ$ . We have also varied the values of scalar linear retardance  $R$  and depolarization parameters  $d_1$  and  $d_2$ . The impact of anisotropy of linear depolarization ( $d_1 \neq d_2$ ) on calculated values of azimuth  $\theta_R$  [Eq. (3)] and  $AoP$  is shown in Fig. 1. The difference between the values of  $\theta_R$  and  $AoP$  is less than  $1^\circ$  for low anisotropy of linear depolarization ( $d_1 - d_2 < 0.1$ ). However, this difference reaches up to  $40^\circ$  for certain values of  $\theta_R$  when  $d_1 - d_2 > 0.8$ .

The values of scalar retardance  $R_{\text{aniso}}$  were calculated using Eq. (4) that accounts for the anisotropy of linear depolarization ( $d_1 \neq d_2$ ) and compared with the calculated values of  $R_{\text{iso}}$  making use of the assumption of isotropic linear depolarization, namely,  $d_1 = d_2$  (or  $|m_{23}| = |m_{32}|$ ) in Eq. (4). The errors in calculated values of  $R_{\text{iso}}$  for a quarter-wave plate may reach  $160^\circ$  at the critical azimuth values of  $\pm 45^\circ$  in the case of strong anisotropy of linear depolarization (see Fig. 2). On the contrary, the values of  $R_{\text{aniso}}$  calculated with Eq. (4) consistently reproduce the retardance of a quarter-wave plate when parameter  $d_2$  ranges from 0.01 to 0.99. Usually, the values of scalar linear retardance measured with complete Mueller polarimetry on thick tissue samples in reflection do not exceed  $90^\circ$  [1, 14]. However, the discrepancy

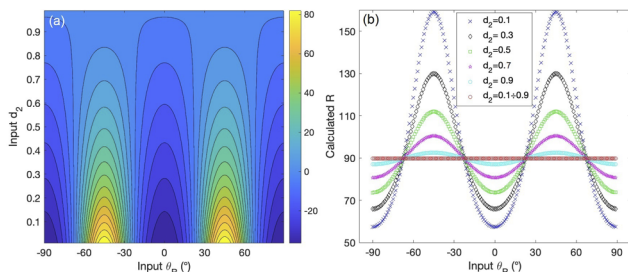


**Fig. 2.** (a) 2D map of calculated  $R_{\text{iso}} - R_{\text{aniso}}$  values at different input values of  $\theta_R$  and  $d_2$ ; (b) calculated values of  $R_{\text{iso}}$  (colored markers) and  $R_{\text{aniso}}$  (red circles) for  $d_2 = 0.1 - 0.9$ . Input linear retardance  $R = 90^\circ$ ,  $d_1 = 0.99$ .

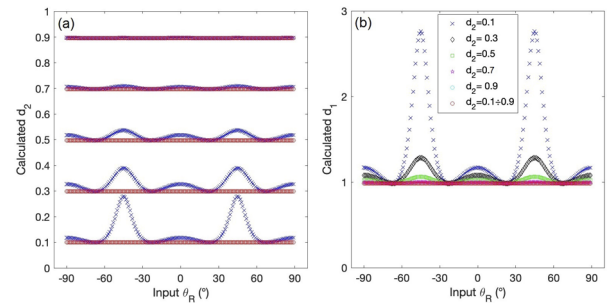


**Fig. 3.** Calculated values of (a)  $d_2(R_{\text{aniso}})$  (red circles) and  $d_2(R_{\text{iso}})$  (blue crosses) at  $d_2 = 0.1 - 0.9$ ; (b)  $d_1(R_{\text{aniso}})$  (red circles) and  $d_1(R_{\text{iso}})$  (colored markers) for  $d_2 = 0.1 - 0.9$ . Input linear retardance  $R = 90^\circ$ ,  $d_1 = 0.99$ .

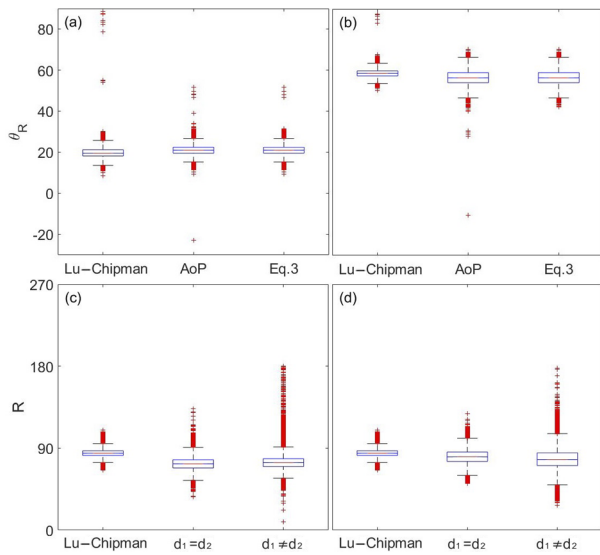
between  $R_{\text{aniso}}$  and  $R_{\text{iso}}$  may still reach several degrees at some azimuth values for media with high anisotropy of linear depolarization (e.g., with presence of non-spherical scatterers). Thus, neglecting this anisotropy may introduce significant errors and produce artifacts in polarimetric images of tissue used for diagnosis. Parameter  $R_{\text{aniso}}$  reproduces correctly the input values of scalar retardance for  $-90^\circ \leq \theta_R \leq 90^\circ$  and  $0.01 \leq d_2 \leq 0.99$ .

Figure 3(a) shows the values of  $d_2$  calculated with Eq. (6) using either  $R_{\text{aniso}}$  or  $R_{\text{iso}}$  values of linear retardance. The former reconstructs correctly the input values of  $d_2$ . When  $d_1 \approx d_2 > 0.9$  the values of  $d_2$  calculated with either  $R_{\text{aniso}}$  or  $R_{\text{iso}}$  values are very close for all angles  $\theta_R$ , while for strong anisotropy of linear depolarization using  $R_{\text{iso}}$  values produces erroneous results for  $d_2$ . The values of parameter  $d_1$  calculated with Eq. (5) using  $R_{\text{iso}}$  values of linear retardance exceed 1 [see Fig. 3(b)], which is non-physical, whereas using the  $R_{\text{aniso}}$  values of linear retardance in Eq. (5) one reproduces correctly the input value of parameter  $d_1 = 0.99$  for all input values of parameters  $\theta_R$  and  $d_2$ . For the sake of completeness we have applied Eqs. (3)–(6) to the MM of the same optical phantom followed by a diattenuator  $\mathbf{M}_D \neq \mathbf{I}$  with low diattenuation value of 0.1. Whereas the calculated values of  $\theta_R$  are not affected, the values of  $R_{\text{aniso}}$ ,  $d_1(R_{\text{aniso}})$  and  $d_2(R_{\text{aniso}})$  have changed in the second decimal digit only. Thus, by measuring the first three rows of MM and accounting for the anisotropy of linear depolarization (if any), one can calculate the orientation of the optical axis, scalar linear retardance, and linear depolarization parameters of a sample.

Next, we measured in reflection configuration the complete MM of tape affixed to a glass slide. Tape was placed sequentially at  $15^\circ$  and  $50^\circ$  with respect to the laboratory reference frame.

All data were acquired with a commercial-grade microscope modified to include MM capability. A typical assembly of rotating elements (quarter-wave plate) and fixed polarizers were used [15] at the source (light emitting diode (LED) at 550 nm, Thorlabs Inc.) and detector (PCO Inc, Germany) to generate the MM using the strategy described in Ref. [16] and were controlled with a custom software (MATLAB). The system was calibrated with the eigenvalue calibration method described elsewhere [17] achieving an average inverse condition number of 0.22 for both polarization state generator and polarization state analyzer. Theoretically this system can achieve a maximum of 0.26.

The values of  $\theta_R$  and  $R$  were calculated with LCPD first. Then we took the first three rows of recorded matrices and calculated the values of  $\theta_R$ ,  $R$ ,  $d_1$ , and  $d_2$  using Eqs. (3)–(6). The boxplots of the distribution of parameters  $\theta_R$  and  $R$  in the corresponding images taken at different orientation of tape are shown in Fig. 4.



**Fig. 4.** Boxplots of the distributions of (a),(b)  $\theta_R$  and (c),(d)  $R$  values calculated with different decompositions of the MM images of tape taken at different orientation of a sample within imaging plane: (a),(c) 15°; (b),(d) 50°.

The median values of the azimuth distributions obtained with LCPD and the values of azimuth calculated assuming either isotropic [Eq. (7)] or anisotropic linear depolarization [Eq. (3)] differ by less than 3° for both tape orientations.

The median values of distributions of  $R$  calculated with LCPD vary within the interval 76°–82° with the change of tape orientation. The corresponding variations of median values of distributions of  $R$  calculated with Eq. (4) assuming either isotropic ( $m_{23} = m_{32}$  or  $d_1 = d_2$ ) or anisotropic ( $m_{23} \neq m_{32}$  or  $d_1 \neq d_2$ ) linear depolarization span over the interval 75°–77°. A large number of outliers is confirmed to arise by the presence of small air bubbles between tape and glass. Whereas the difference in

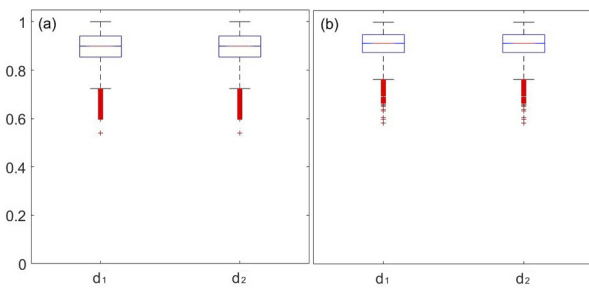


**Fig. 5.** Boxplots of  $d_1$  and  $d_2$  values calculated with Eqs. (5) and (6) from 3 × 4 MM images of tape taken at different orientation of a sample within imaging plane: (a) 15°; (b) 50°.

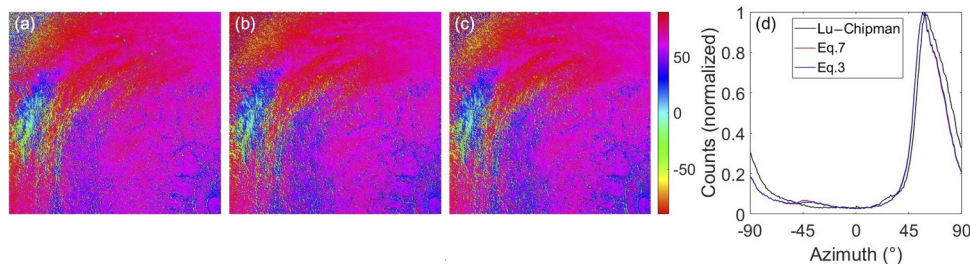
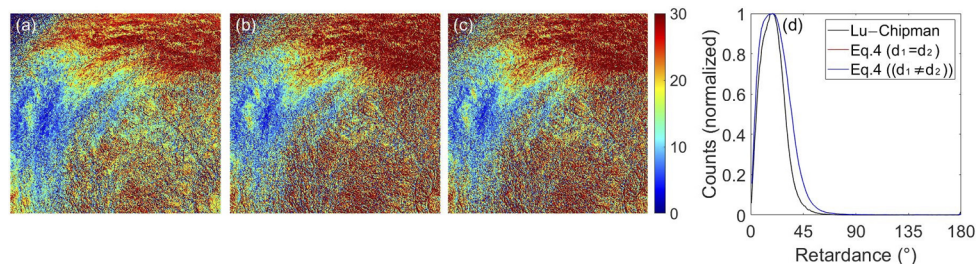


**Fig. 6.** Images (1 × 1.15 mm<sup>2</sup>) of  $\theta_R$  calculated with: (a) LCPD of complete MM; (b) Eq. (3) (3 × 4 MM); (c) Eq. (7) (Stokes polarimetry); (d) normalized histograms of  $\theta_R$  for all three decompositions.

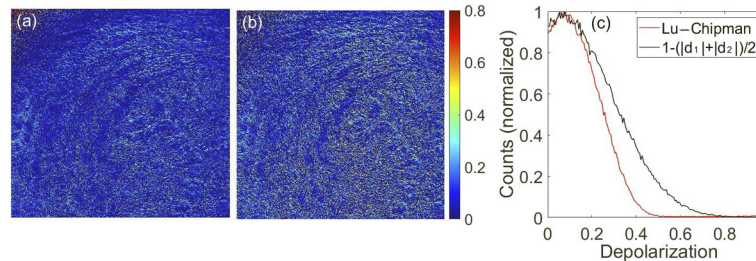
calculated values of linear retardance is not negligible, it is worth mentioning that all discussed approaches provide a practical estimation of a sample retardance, because they assume the sequential order of polarimetric effects (which is not the case for heterogeneous samples) and perform a non-linear compression of data.

Figure 5 shows the boxplots of the distributions of parameters  $d_1$  and  $d_2$  calculated with Eqs. (5) and (6). The median values of both  $d_1$  and  $d_2$  vary between 0.89 and 0.91, meaning that depolarization of tape is not high. The difference between the median values does not exceed 0.02 at any sample orientation indicating very weak anisotropy of linear depolarization.

The final test was performed using the experimental back-scattered MM images of a 50 μm-thick section of mouse uterine cervix. Collagen is the main constituent of the uterine cervix and is arranged circumferentially around the cervical canal [18,19]. The presence of aligned collagen fibers induces tissue birefringence. Figure 6 shows the images of  $\theta_R$  for cervical tissue calculated with LCPD and Eq. (3) assuming either anisotropy ( $m_{23} \neq m_{32}$ ) or isotropy ( $m_{23} = m_{32}$ ) of linear depolarization. All azimuth maps demonstrate a compelling correlation. The histograms of  $\theta_R$  values calculated with LCPD and Eq. (3) assuming either isotropy or anisotropy of linear depolarization are very close. It suggests that linear depolarization by cervical tissue is invariant under rotation of a sample in the imaging plane. The difference in  $\theta_R$  values calculated with LCPD and Eqs. (3) and (7) does not exceed a few degrees, being maximal at azimuth values close to ±90°. The maps of linear retardance  $R$  and corresponding histograms are shown in Fig. 7. The retardance values calculated with LCPD and Eq. (4) for either isotropic or anisotropic linear depolarization are again very close in value; the structural morphology of cervical tissue is reproduced accurately in all images. High values of linear retardance (up to 30°), are observed at the top of each image along the arc, corresponding to the zone of a densely packed collagen fibers aligned around the cervical canal. The drop of retardance values to 5°–7° at the left-hand zone of each image is likely related to the drop of a collagen fibers density. The map of total depolarization calculated with LCPD is shown in Fig. 8(a). The map of equivalent metric of linear depolarization  $1 - (|d_1| + |d_2|)/2$  is presented in Fig. 8(b). The histograms of the corresponding distributions of depolarization values [Fig. 8(c)] demonstrate peak at low depolarization of 0.1. This is related to low number of scattering events within a thin layer of tissue. Figure 8(c) shows a slightly higher number of pixels with the depolarization values between 0.2 and 0.8 for the linear depolarization metrics calculated with Eqs. (5) and (6) compared with the total depolarization from LCPD. Hence, the contrast is higher in Fig. 8(b) compared with Fig. 8(a), but the structural morphology of tissue is clearly distinguishable in both images. The distributions of both parameters  $d_1$  and  $d_2$  are identical, meaning that linear depolarization is isotropic for cervical tissue.



**Fig. 7.** Images ( $1 \times 1.15 \text{ mm}^2$ ) of linear retardance  $R$  calculated with: (a) LCPD of complete MM; (b)  $R_{\text{iso}}$ , Eq. (4); (c)  $R_{\text{aniso}}$ , Eq. (4); (d) normalized histograms of linear retardance distributions in (a)–(c).



**Fig. 8.** Images ( $1 \times 1.15 \text{ mm}^2$ ) of depolarization calculated with: (a) LCPD of complete MM; (b)  $1 - (|d_1| + |d_2|)/2$ , parameters  $d_1$  and  $d_2$  are from Eqs. (3) and (4); (c) normalized histograms of the depolarization distributions in (a) and (b).

Generating the maps of linear retardance, azimuth, and depolarization from MM images of biological tissue has been shown to have a diagnostic value (e.g., pre-term labor risk assessment [4], visualization of brain tumor borders [14], etc.). The optical diagnosis of pathological changes in tissue is often based not on the exact values of polarimetric parameters but rather on their relative changes with respect to those for healthy tissue. We expect that slight widening of polarimetric parameters distributions obtained with a simplified approach should not affect significantly the contrast in polarimetric images at macro-scale.

We have tested the simplified approach on simulated data and experimental data for optical phantom and cervical tissue by calculating the polarimetric parameters using only part of a MM. Our results show good agreement with the input parameters of theoretical model and the parameter values obtained with LCPD of the complete MM. Our findings open an avenue for developing medical imaging with partial polarimeters (e.g.,  $3 \times 4 \text{ MM}$  [8,10] or Stokes polarimeters [11,20]) that may provide a good compromise between the simplicity, compactness, speed of the instrument, and the accuracy of polarimetric measurements required for medical diagnosis.

**Funding.** National Science Foundation (1548924 STC:STROBE).

**Acknowledgments.** Ecole Polytechnique program “Invited Professors”. A. Ajmal for aid in capturing the MM images of tape and cervix. We acknowledge partial support from Dr. Herbert and Nicole Wertheim Family Foundation.

**Disclosures.** The authors declare no conflicts of interest.

**Data availability.** Data underlying the results presented in this paper are not publicly available at this time but may be obtained from the authors upon reasonable request.

## REFERENCES

- M. Kupinski, M. Boffety, F. Goudail, R. Ossikovski, A. Pierangelo, J. Rehbinder, J. Vizet, and T. Novikova, *Biomed. Opt. Express* **9**, 5691 (2018).
- M. H. Smith, A. Lompadó, and P. Burke, *Proc. SPIE* **3911**, 210 (2000).
- A. Pierangelo, S. Manhas, A. Benali, M.-R. Antonelli, T. Novikova, P. Validire, B. Gayet, and A. D. Martino, *Proc. SPIE* **7895**, 78950E (2011).
- J. Chue-Sang, N. Holness, M. Gonzalez, J. Greaves, I. Saytashev, S. Stoff, A. Gandjbakhche, V. V. Chernomordik, G. Burkett, and J. C. Ramella-Roman, *J. Biomed. Opt.* **23**, 1 (2018).
- R. A. Chipman, in *Handbook of Optics*, Vol. II, Chap. 22, 2nd ed. (McGraw-Hill, Inc., New York, 1995).
- S. Y. Lu and R. A. Chipman, *J. Opt. Soc. Am. A* **13**, 1106 (1996).
- S. R. Cloude, *Optik* **75**, 26 (1986).
- M. Gonzalez, R. Ossikovski, T. Novikova, and J. C. Ramella-Roman, *J. Phys. D: Appl. Phys.* **54**, 424005 (2021).
- A. Vitkin, N. Ghosh, and A. De Martino, in *Photonics: Biomedical Photonics Spectroscopy, and Microscopy* (John Wiley & Sons, Inc., 2015).
- T. Boonya-ananta, M. Gonzalez, V. N. Du Le, E. DeHoog, M. J. Paidas, A. Jayakumar, and J. C. Ramella-Roman, *Proc. SPIE* **11963**, TM4B.3 (2022).
- J. Qi, M. Ye, M. Singh, N. T. Clancy, and D. S. Elson, *Biomed. Opt. Express* **4**, 2433 (2013).
- O. Arteaga and R. Ossikovski, *J. Opt. Soc. Am. A* **36**, 416 (2019).
- Y. Chen, Z. Zhu, Z. Liang, L. E. Iannucci, S. P. Lake, and V. Gruev, *OSA Continuum* **4**, 1461 (2021).
- P. Schucht, H. R. Lee, M. H. Mezouar, E. Hewer, A. Raabe, M. Murek, I. Zubak, J. Goldberg, E. Kövari, A. Pierangelo, and T. Novikova, *IEEE Trans. Med. Imaging* **39**, 4376 (2020).
- Z. Chen, R. Meng, Y. Zhu, and H. Ma, *Opt. Lasers Eng.* **129**, 106055 (2020).
- J. Soni, H. Purwar, H. Lakhota, S. Chandel, C. Banerjee, U. Kumar, and N. Ghosh, *Opt. Express* **21**, 15475 (2013).
- E. Compain, S. Poirier, and B. Drevillon, *Appl. Opt.* **38**, 3490 (1999).
- H. R. Lee, I. Saytashev, V. N. D. Le, M. Mahendroo, J. C. Ramella-Roman, and T. Novikova, *Sci. Rep.* **11**, 15621 (2021).
- J. Chue-Sang, Y. Bai, S. Stoff, M. Gonzalez, N. Holness, J. Gomes, R. Jung, A. Gandjbakhche, V. V. Chernomordik, and J. C. Ramella-Roman, *J. Biomed. Opt.* **22**, 100430U (2017).
- L. E. Iannucci, M. B. Riak, and S. P. Lake, *Proc. SPIE* **11963**, 4 (2022).